

Surface Vision Mamba: Leveraging Bidirectional State Space Model for Efficient Spherical Manifold Representation

Rongzhao He¹, Weihao Zheng^{1*}, Leilei Zhao², Ying Wang¹, Dalin Zhu³, Dan Wu^{4*}, Bin Hu^{1,5,6*}

¹ School of Information Science and Engineering, Lanzhou University, Lanzhou, Gansu, China

² School of Computer Science and Technology, Harbin Institute of Technology, Shenzhen, China

³ Medical imaging center, Gansu Maternity and Child-care Hospital (Gansu Provincial Central Hospital)

⁴ Key Laboratory for Biomedical Engineering of Ministry of Education, Department of Biomedical Engineering, College of Biomedical Engineering & Instrument Science, Zhejiang University, Hangzhou, Zhejiang, China

⁵ School of Medical Technology, Beijing Institute of Technology, Beijing, China

⁶ CAS Center for Excellence in Brain Science and Intelligence Technology, Shanghai Institutes for Biological Sciences, Chinese Academy of Sciences, Shanghai, China

* **Correspondence:** {zhengweihao, bh}@lzu.edu.cn (W. Zheng, B. Hu); danwu.bme@zju.edu.cn (D. Wu)

Abstract

Attention-based methods have demonstrated exceptional performance in modelling long-range dependencies on spherical cortical surfaces, surpassing traditional Geometric Deep Learning (GDL) models. However, their extensive inference time and high memory demands pose challenges for application to large datasets with limited computing resources. Inspired by the state space model in computer vision, we introduce the attention-free Vision Mamba (Vim) to spherical surfaces, presenting a domain-agnostic architecture for analyzing data on spherical manifolds. Our method achieves surface patching by representing spherical data as a sequence of triangular patches derived from a subdivided icosphere. The proposed Surface Vision Mamba (SiM) is evaluated on multiple neurodevelopmental phenotype regression tasks using cortical surface metrics from neonatal brains. Experimental results demonstrate that SiM outperforms both attention- and GDL-based methods, delivering 4.8 times faster inference and achieving 91.7% lower memory consumption compared to the Surface Vision Transformer (SiT) under the Ico-4 grid partitioning. Sensitivity analysis further underscores the potential of SiM to identify subtle cognitive developmental patterns. The code is available at <https://github.com/Rongzhao-He/surface-vision-mamba>.

1. Introduction

Many methods have been developed for traditional Euclidean space data, such as Convolution Neural Networks (CNNs) and attention-based [5, 6] approaches. CNNs use a regular convolutional kernel to slide over the input data, calculating the weighted sum at each location, while attention-based methods treat the data as a sequence of patches. However, few models exist for non-Euclidean space data consist of graph, manifold and hyperbolic space data which have more complex geometries and distance metrics. These types of data are typically crucial in domains such as neuroscience, social network analysis, and theoretical physics, where their unique structures provide rich but underutilized information.

Existing methods for processing non-Euclidean data can be broadly categorized into attention-based and Geometric Deep Learning (GDL)-based [7, 8] methods. Attention-based methods are effective in capturing long-range dependencies but are constrained in resource limited situations due to the quadratic complexity of the attention mechanism concerning sequence length, leading to higher memory consumption and slower inference time. Conversely, GDL-based methods, which operate directly on non-Euclidean data, are effective in handling complex geometric topology structure and distance metrics.

However, they fail to extract global patterns, especially when applied to large-scale and highly intricate data, resulting in diminished performance. Thus, a key challenge for processing non-Euclidean data lies in improving efficiency while maintaining relatively excellent performance.

With the emergence of *State Space Models* (SSMs) [9], traditional sequence modeling methods have been revitalized, demonstrating promising capabilities for efficient representation learning. A recent variant, Mamba [10], has significantly surpassed traditional SSMs by integrating a selective scan mechanism that adapts parameters based on input and using a hardware-aware algorithm to parallelize scanning, thereby reducing memory I/O for more efficient inference. Motivated by models like ViT [11] and ViG [12], [13] adapted Mamba to computer vision, introducing a bidirectional SSM structure to address direction-sensitive challenges, termed Vision Mamba (Vim).

Non-Euclidean data, particularly spherical cortical surface data, is characterized by high resolution, rich features, and intricate geometric shapes, as the cortical surface is inherently a high-dimensional manifold. While these data provide valuable insights into neurodevelopment, their effective representation poses a formidable challenge, often requiring a balance between performance and computational efficiency. Inspired by the efficiency of Vim, we extend its application to cerebral cortex analysis—an important yet underexplored area—by proposing Surface Vision Mamba (SiM). To adapt SiM to the unique characteristics of cortical surface data, we adjusted the input sequence length using various surface patching methods, as illustrated in Figure 1.

The main contributions of this study can be summarized as follows:

1. We introduce SiM, an adaptation of Vim, as a generic backbone network for analyzing data mapped onto genus-zero surfaces.
2. Leveraging the suitability of Mamba for tasks with *long-sequence* and *autoregressive* characteristics [14], we explore the impact of varying input sequence length on surface data in non-Euclidean space. We further implement autoregressive pretraining to validate the effectiveness of this approach.
3. Extensive experiments on three neurodevelopmental phenotype regression tasks, including the prediction of postmenstrual age (PMA) and long-term language and motor outcomes, demonstrate that our proposed SiM achieves promising performance compared to attention- and GDL-based models and is $4.8\times$ faster than SiT and saves 91.7% GPU memory when performing batch inference under the Ico-4 grid partitioning.

2. Related Work

2.1. Geometric Deep Learning

Geometric Deep Learning (GDL) has emerged as a powerful tool for analyzing irregular geometries. While traditional CNNs specialize in processing Euclidean data, such as images, they are less effective for irregular data (e.g., cortical surfaces). GDL models extend CNNs to non-Euclidean domains, enabling the capture of intricate topological and geometric properties of the cortex. While these models excel in capturing local features, they often face challenges in learning long-range dependencies due to high computational costs or inherent architectural limitations, limiting their ability to model more complex relationships. Systematic comparisons of various GDL methods, such as MoNet [15] and Spherical UNet [16], in brain phenotype prediction tasks have stressed these challenges.

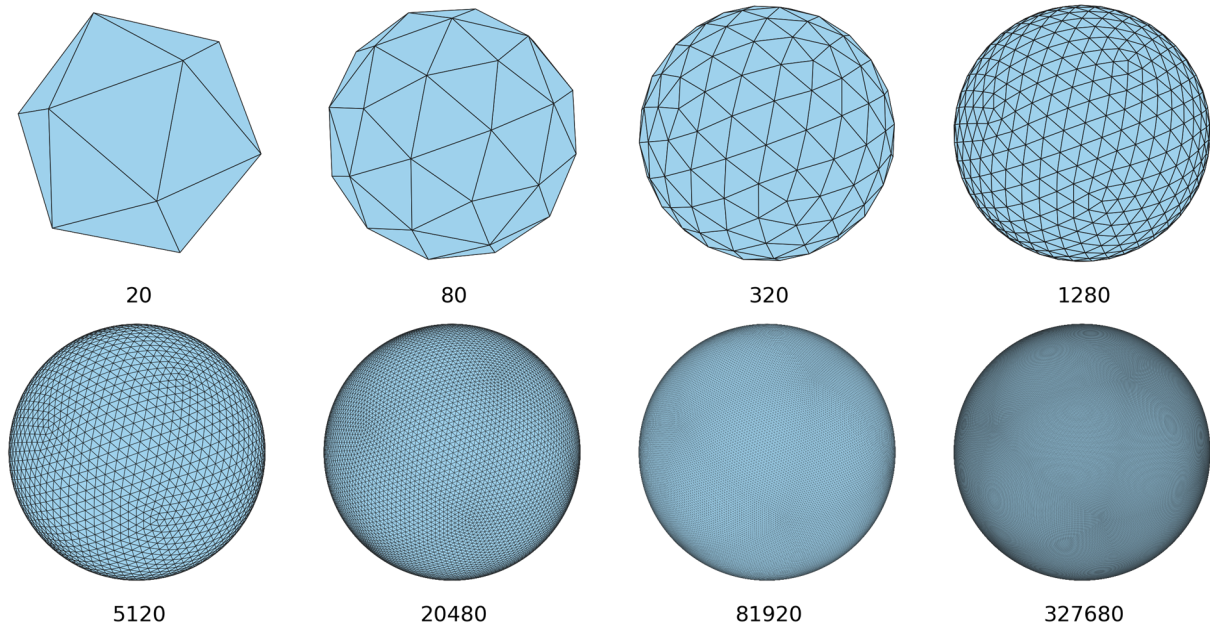


Figure 1. Representative icosahedron discretized spherical surfaces with sequential subdivisions. The number of faces of each spherical surface is denoted under the surface.

2.2. Attention-based methods

The self-attention mechanism, introduced in the Transformer [17], has revolutionized natural language processing (NLP) by capturing long-range dependencies. This architecture became the foundation for models like BERT [18] and GPT [19]. Researchers extended self-attention to visual representation learning by splitting image into patches, known as the Vision Transformer (ViT) [11]. The Swin Transformer [20] proposed hierarchical image merging via shifted windows, significantly improving efficiency and scalability for tasks like object detection and image segmentation. In medical image tasks, Surface Vision Transformer (SiT) [5] was proposed to address irregular geometries, such as the cerebral cortex. Motivated by the asymmetric development of brain structure, the hemispheric relation inference network (HRINet) [6] was designed to extract potential covariation relationships between bilateral hemispheres. However, the attention-based models not only struggle with quadratic time complexity relative to the sequence length, leading to significant computational costs in modeling dense, long sequences in NLP and high-resolution images in computer vision, but are also limited by quadratic space complexity owing to store all key-value pairs from previous sequences as its memory. To address these issues, numerous works have focused on reducing both quadratic time complexity and memory cost, as demonstrated in [21-29] by changing the operation of attention calculation, but cause a drop in performance.

2.3. State Space Models (SSMs)

The SSMs have recently been proposed to address key limitations of Recurrent Neural Networks (RNNs) [30], particularly the challenges of non-parallelizable training and the tendency to forget earlier information as sequence length increases. The structured state space for sequence (S4) [9] employs the zero-order hold technique for discretization and High-order Polynomial Projection Operators (HiPPO) [31] to compress context into a smaller state. However, S4 is constrained by Linear Time Invariance (LTI), leading to limited ability to perform adaptive inference based on different inputs. In addition, S4 fails to prioritize and attend to the most critical parts owing to treat each segment equally. To overcome these challenges, Mamba [10] incorporates a selective scanning mechanism to selectively extract relevant

information depending on the inputs. Vim [13] extended capabilities of Mamba to the computer vision, designing a generic vision backbone based on bidirectional SSM to address direction-sensitive problem, analogous to the ViT. Additionally, the Visual State Space Model (VMamba) [32] proposed a cross-scan module to bridge the difference between 1D array scanning and 2D plane traversal, enabling the adaptation of Mamba for visual data while preserving the size of the receptive fields.

3. Materials and Methods

3.1. Image acquisition and Dataset

Table 1. Demographic and clinical information of the subjects.

	<i>dHCP</i>			<i>Replication dataset</i>
	<i>Subset 1 (N=408)</i>	<i>Subset 2 (N=16)</i>	<i>Subset 3 (N=410)</i>	<i>(N=10)</i>
Birth age [weeks^{+days}], median (IQR)	39 ⁺⁴ (38 ⁺⁶ - 40 ⁺⁶)	30 ⁺⁴ (28 ⁺⁰ - 32 ⁺⁴)	38 ⁺⁶ (38 ⁺³ - 40 ⁺⁵)	37 ⁺² (35 ⁺⁴ - 39 ⁺⁰)
Scan age [weeks^{+days}], median (IQR)	40 ⁺⁶ (39 ⁺⁴ - 42 ⁺²)	41 ⁺⁴ (38 ⁺³ - 43 ⁺⁶)	41 ⁺¹ (40 ⁺⁰ - 42 ⁺³)	39 ⁺⁴ (39 ⁺² - 40 ⁺⁵)
Birth weight, mean (SD)	3.28 (0.32)	1.52 (0.36)	3.11 (0.64)	2.69 (0.78)
Head circumference at scan¹, mean (SD)	34.81 (3.40)	34.85 (9.33)	34.99 (3.26)	-
Radiology score (1/2/3/4/5)	295/174/0/0/0	3/3/5/1/4	203/129/47/9/22	-
Gender (M/F)	225/183	9/7	210/200	4/6
Language, mean (SD)	-	-	19.42 (5.26)	-
Motor, mean (SD)	-	-	20.55 (3.17)	-

Note: ¹ 14, 1 and 15 head circumference data were missed in *Subset 1*, *Subset 2*, and *Subset 3*, respectively. The unit is centimeters. IQR and SD denote interquartile range and standard deviation, respectively.

The imaging data used in this work are from the publicly available Developing Human Connectome Project (dHCP) and the Gansu Provincial Maternity and Child-care Hospital (GPMCH). We used T1-weighted (T1w) and T2-weighted (T2w) images to calculate morphometric metrics of cerebral cortex.

The dHCP is approved by the United Kingdom Health Research Ethics Authority (reference number: 14/LO/1169). Additionally, we collected T1w and T2w images of 10 infants from the GPMCH (2020-GSFY-05). These images were acquired in the resolution of $0.8 \times 0.8 \times 1.6 \text{ mm}^3$ with 0.8 mm overlap, and were reconstructed to 0.5 mm isotropic resolution.

Concerning the data from dHCP, a total of 516 infants covering preterm- and term-born neonates ranging from 24 to 45 weeks postmenstrual age (PMA) are enrolled in our study. The neurodevelopmental assessments for these infants, conducted at 18 months of age using the Bayley-III Scales of Infant Development, can also be obtained. We used the following exclusion criteria: For PMA prediction, (i) we excluded the later scans of infants who were scanned twice to avoid the influence of extrauterine environmental factors; (ii) term-born neonates with focal abnormalities (radiology score > 2) were excluded to build a normative model for normal brain development assessment. The remaining infants were then split into two subsets: *Subset 1*: 408 participants who were born and scanned between 34 and 45 PMA; *Subset 2*: 16 preterm infants who were born before 34 PMA and scanned at term-equivalent age (> 37 PMA) for the evaluation of premature effects on brain development. For language and motor scores prediction, we retained the scans closest to 40 weeks for neonates scanned twice identified as *Subset 3*: 410 infants born between 23 and 43 gestational weeks (GA). We further utilized data from GPMCH as a *Replication dataset*, consisting of 10 neonates born and scanned between 34 and 40 PMA, to evaluate the generalization ability of the models. The demographic details are provided in Table 1.

Four cortical surface metrics—curvature, sulcal depth, cortical thickness, and myelination (T1w/T2w ratio)—were used as features. Each feature channel was normalized using Z-score. *Subset 1* and *3* were

split into training, validation, and testing datasets in an 8:1:1 ratio within each label interval. Data from the four subsets were registered to the dHCP 40-week spherical template, which represents the cortical surface as an approximated sphere composed of triangles, with 32,492 vertices per hemisphere. We resampled the template sphere to a regular sixth-order icosphere (Ico-6) using barycentric interpolation.

3.2. Preliminaries

SSMs are generally considered linear time-invariant (LTI) systems that map an input stimulation $u(t) \in \mathbb{R}^N$ to an output response $y(t) \in \mathbb{R}^N$ through a hidden state $h(t) \in \mathbb{R}^N$. The evolution of the hidden state over time is governed by parameter matrices $\mathbf{A} \in \mathbb{R}^{N \times N}$, $\mathbf{B} \in \mathbb{R}^{N \times 1}$, and $\mathbf{C} \in \mathbb{R}^{1 \times N}$. The system is mathematically described using a linear ordinary differential equation (ODEs) as follows:

$$\begin{aligned} h'(t) &= \mathbf{A}h(t) + \mathbf{B}u(t) \\ y(t) &= \mathbf{C}h(t) \end{aligned} \quad (1)$$

where \mathbf{A} is the state matrix to control the latent state h , \mathbf{B} denotes the control matrix, and \mathbf{C} is the output matrix. Equation (1) aims to predict the state of the system based on observed data. Since the input is generally continuous, the primary use of SSMs is in continuous-time representation. However, since computers struggle with processing continuous signals and the real data we used is typically discrete rather than continuous, the standard procedure is to discretize Equation (1) using the Zero-order hold (ZOH) technique. This method assumes that the input signal remains constant between sampling intervals, which can be formulated as follows:

$$\begin{aligned} h_t &= \bar{\mathbf{A}}h_{t-1} + \bar{\mathbf{B}}u_t \\ y_t &= \mathbf{C}h_t \end{aligned} \quad (2)$$

where $\bar{\mathbf{A}} = \exp(\Delta\mathbf{A})$ and $\bar{\mathbf{B}} = (\Delta\mathbf{A})^{-1}(\exp(\Delta\mathbf{A}) - I) \cdot \Delta\mathbf{B}$ are the discretized parameter matrices and Δ is the discretization step size. The output y is then calculated using a global convolution kernel $\bar{\mathbf{K}} \in \mathbb{R}^L$, L is the input sequence length. The kernel is defined as:

$$\begin{aligned} \bar{\mathbf{K}} &= (\mathbf{C}\bar{\mathbf{B}}, \mathbf{C}\bar{\mathbf{A}}\bar{\mathbf{B}}, \dots, \mathbf{C}\bar{\mathbf{A}}^k\bar{\mathbf{B}}, \dots) \\ y &= u * \bar{\mathbf{K}} \end{aligned} \quad (3)$$

where $k \in [0, L)$ indicates the sequence index.

Mamba addressed key challenges in sequence modeling through a selective scanning mechanism and a faster hardware-aware algorithm. The selective scanning mechanism prioritizes and extracts the most significant information from sequence contexts, compressing it into a refined state and avoiding the inefficiency of treating all elements equally. The hardware-aware algorithm optimizes computational efficiency by leveraging modern hardware capabilities, enabling sub-quadratic time complexity. These characteristics make Mamba highly effective and scalable for processing long sequences while maintaining accuracy and computational efficiency.

3.3. Surface Vision Mamba

Given the interconnected nature of brain, alterations within one region will inevitably influence others. To capture these long-range dependencies, we proposed the SiM model, as shown in Figure 2. Notably, the input domain is divided into $2N$ patches, represented as $\tilde{X} = \{\tilde{L}, \tilde{R} | \tilde{L} \in \mathbb{R}^{N \times V \times C}, \tilde{R} \in \mathbb{R}^{N \times V \times C}\}$, that V is the number of vertices in a patch, and C denotes the number of feature channels. This is then flattened to $X = \{L, R | L \in \mathbb{R}^{N \times (VC)}, R \in \mathbb{R}^{N \times (VC)}\}$. Next, we projected X into D -dimensional vectors using a trainable fully connected layer. Following the design of ViT and BERT, a learnable class token

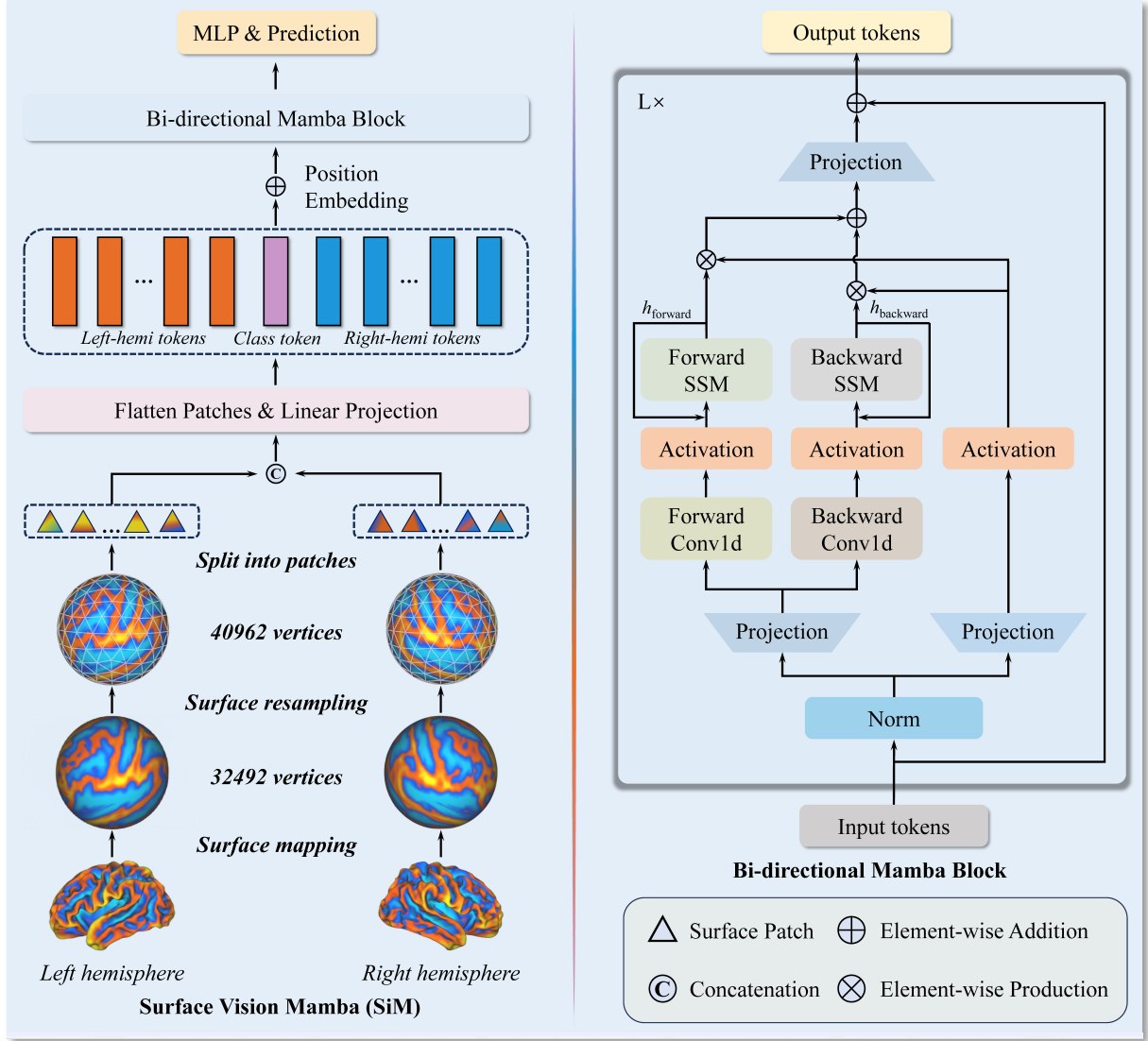


Figure 2. Overview of the proposed Surface Vision Mamba (*SiM*) architecture. The cortical data from the left and right hemispheres are initially mapped onto a 40-week spherical template with 32,492 vertices per hemisphere. The template is then resampled to a sixth-order icosphere containing 40,962 vertices, partitioned into triangular patches (taking Ico-2 shown as an example in the Figure 1) that fully cover the sphere. Surface patches from both hemispheres are concatenated, flattened, and linearly embedded. A learnable class token is inserted between the tokens from the left and right hemispheres, followed by the addition of positional embeddings. The processed data is then fed into the Bi-directional Mamba block.

\mathbf{X}_{cls} is concatenated between the left and right hemispheres to represent the patch sequence. To retain positional information, standard 1D position embeddings \mathbf{E}_{pos} are added to the patch features.

$$\mathbf{S}_0 = [\mathbf{X}_L^1 \mathbf{W}; \dots; \mathbf{X}_L^N \mathbf{W}; \mathbf{X}_{cls}; \mathbf{X}_R^1 \mathbf{W}; \dots; \mathbf{X}_R^N \mathbf{W}] + \mathbf{E}_{pos}, \mathbf{W} \in \mathbb{R}^{(VC) \times D}, \mathbf{E}_{pos} \in \mathbb{R}^{(2N+1) \times D} \quad (4)$$

where $\mathbf{S}_0 \in \mathbb{R}^{(2N+1) \times D}$ is the initial input of *SiM*, \mathbf{X}_L^1 and \mathbf{X}_R^1 represent the first patches of the left and right hemispheres, respectively. The implementation of *SiM* follows the same structure as *Vim*. Specifically, for a given layer l , the input from the previous layer \mathbf{S}_{l-1} is processed as follows:

$$\begin{aligned} \mathbf{S}_l &= \text{SiM}(\mathbf{S}_{l-1}) + \mathbf{S}_{l-1} \\ \mathbf{T} &= \text{LayerNorm}(\mathbf{S}_l^N) \\ \hat{\mathbf{p}} &= \text{MLP}(\mathbf{T}) \end{aligned} \quad (5)$$

Table 2. Summary of the parameters for icospheres of different orders.

Icosphere Order	First	Second	Third	Fourth	Fifth
The number of patches (N)	80	320	1280	5120	20480
The number of vertices(V)	561	153	45	15	6
Input Dimension (VC)	2244	612	180	60	24
Sequence Length ($2N$)	160	640	2560	10240	40960
Icosphere Input Size	160×2244	640×612	2560×180	10240×60	40960×24

3.4. Surface Patching Methods

The choice of surface patching methods can significantly affect model performance. In most *Surface*-based visual tasks, each face of a second-order icosphere (Ico-2) is commonly used as a patch, with all data points in the face treated as vertices. This approach splits the surface into 320 non-overlapping patches, each containing 153 vertices, with patches sharing only common edges. As Mamba has been indicated to perform well on tasks involving long-sequences [14], we extend the sequence length by progressively subdividing the icosahedron into finer discrete levels and evaluate different surface patching methods, including first- to third-order icosphere, as summarized in Table 2. The icosphere subdivision process involves three steps: (i) new vertices are inserted at the midpoints of edges from the previous subdivision level; (ii) new edges are generated between adjacent new vertices within the same face; and (iii) the newly added vertices are projected onto the circumsphere of the icosahedron. The different surface patching methods are visually represented in Figure 1. To address the impact of patching methods, we use the Mean Absolute Error (MAE) as a performance metric and the Multiply-Accumulate Operations (MACs) is used to estimate computational cost.

3.5. Training Methods

Medical imaging datasets are often smaller than natural imaging datasets due to ethical, privacy, and legal restrictions on image acquisition, the variability in imaging equipment and parameter settings, and the challenges of annotating large datasets. To overcome these limitations, pretraining methods are essential for learning robust features, enhancing performance on downstream tasks. In this study, we explore three training strategies: (i) training models from scratch; (ii) fine-tuning pretrained weights from ImageNet (as released in Vision Mamba); and (iii) self-supervised pretraining for visual representation learning. Given the suitability of the Mamba architecture for autoregressive modeling [33], we adopt autoregressive approach for self-supervised pretraining, where the model predicts the next token based on preceding information. The performance of all three training strategies is evaluated using mean squared error (MSE) as the loss function.

4. Results and Discussion

4.1. Model Variants

The proposed SiM configurations are built upon three variants of Vim: Vim-Tiny, Vim-Small, and Vim-Base. Table 3 summarizes the architectural details of SiM, employing concise notations for model size

Table 3. The configuration of different architecture variants.

Model	Layers	Hidden size D	Expanded size E	Parameters
SiM-Tiny	24	192	384	7M
SiM-Small	24	384	768	24M
SiM-Base	24	768	1536	93M

Table 4. Performance comparison on dHCP.

Methods	Supervised		Fine-tuning		Autoregressive		Params. (M)	MACs (G)
	MAE	MSE	MAE	MSE	MAE	MSE		
MoNet	0.64±0.54	0.70±1.37	-	-	-	-	-	-
S2CNN [1]	0.69±0.45	0.69±0.73	-	-	-	-	-	-
ChebNet [2]	0.71±0.59	0.85±1.14	-	-	-	-	-	-
GConvNet [3]	0.86±0.73	1.27±1.91	-	-	-	-	-	-
PointNet++ [4]	0.67±0.07	0.76±0.10	-	-	-	-	-	-
Spherical UNet	0.72±0.58	0.85±1.31	-	-	-	-	-	-
HRINet/1	0.75±0.67	1.05±0.05	-	-	-	-	10	-
SiT-Tiny/1	0.79±0.62	1.04±0.42	0.81±0.59	1.37±0.46	-	-	6	0.9
SiT-Small/1	0.81±0.57	1.06±0.36	0.87±0.63	0.93±0.28	-	-	22	3.6
SiT-Base/1	0.82±0.56	0.98±0.33	0.86±0.74	1.13±0.47	-	-	87	14.0
SiM-Tiny/1	0.85±0.64	0.91±0.31	0.76±0.66	1.21±0.26	1.03±0.70	1.87±0.42	7	1.9
SiM-Small/1	0.87±0.74	1.60±0.38	0.76±0.69	1.55±0.64	1.26±0.83	2.43±0.20	24	4.2
SiM-Base/1	0.86±0.69	1.20±0.04	0.84±0.63	1.24±0.19	1.06±0.67	1.34±0.30	92	15.4
HRINet/2	0.62±0.44	0.39±0.25	-	-	-	-	10	-
SiT-Tiny/2	0.69±0.52	0.47±0.36	0.66±0.58	0.78±0.01	-	-	6	3.5
SiT-Small/2	0.67±0.50	0.62±0.11	0.65±0.46	0.65±0.03	-	-	22	13.9
SiT-Base/2	0.64±0.57	0.57±0.55	0.72±0.47	0.58±0.20	-	-	86	55.0
SiM-Tiny/2	1.09±0.80	2.00±0.22	0.74±0.59	0.98±0.10	1.04±0.77	2.19±0.65	6	4.7
SiM-Small/2	0.98±0.80	1.89±0.38	0.60±0.49	0.52±0.10	1.12±0.92	3.50±1.79	24	16.5
SiM-Base/2	0.88±0.66	1.27±0.09	0.74±0.68	0.89±0.15	1.20±0.83	3.17±1.33	91	61.5
HRINet/3	<i>OOM</i>	<i>OOM</i>	-	-	-	-	-	-
SiT-Tiny/3	0.60±0.48	0.47±0.16	0.62±0.50	0.53±0.13	-	-	6	14.4
SiT-Small/3	0.60±0.51	0.54±0.41	0.60±0.43	0.42±0.16	-	-	22	56.1
SiT-Base/3	<i>OOM</i>	<i>OOM</i>	<i>OOM</i>	<i>OOM</i>	-	-	87	220.9
SiM-Tiny/3	1.09±0.76	2.79±1.30	0.60±0.46	0.85±0.35	0.91±0.81	3.62±2.73	7	18.9
SiM-Small/3	1.09±0.84	1.78±0.14	0.56±0.50	0.59±0.04	0.87±0.65	1.89±0.91	24	66.1
SiM-Base/3	1.03±0.81	2.30±0.73	0.62±0.45	0.65±0.07	1.09±0.71	2.27±0.76	93	245.5

Note: Case marked as ('-') represents unspecified values. ('OOM') means out of memory. Bold intricates the best performance in MAE and MSE, respectively. The detailed setup is provided in A.1.

and surface patching methods. For instance, SiM-B/3 refers to the “Base” variant with an input size of 2560×180 , using an Ico-3 grid. With the constant resolution of Ico-6, higher-order icospheres yield finer-grained patches, enabling more precise analysis. This capability is peculiarly valuable in medical imaging, where finer-grained insights are critical for capturing subtle variations related to diseases.

4.2. Infant brain age prediction

As shown in Table 4, the comparison results of SiM models against benchmark GDL models [7, 8] and attention-based methods [5, 6] on PMA prediction of *Subset 1* on the three training strategies (see section 3.5). Notably, when fine-tuning with ImageNet pretraining weights, three variants of SiM outperform all the GDL models using an Ico-3 grid. With comparable model parameters and MACs, SiM-S/3 achieves a performance of 0.56 ± 0.50 , surpassing SiT-S/3 (0.60 ± 0.43). However, when training from scratch, the performance of all SiM variants decreased obviously, likely reflecting a tendency to overfit on small datasets due to the absence of strong prior weights, resulting in performance degradation. Although self-supervised pretraining has been shown to effectively strengthen model performance in previous studies, this benefit is less evident in our results. Actually, only the SiM-T/3 and SiM-S/3 exhibit improvements compared to training from scratch. This may be attributed to overfitting, which hampers generalization, or to the limited sample size, restricting the ability of model to capture sufficient features.

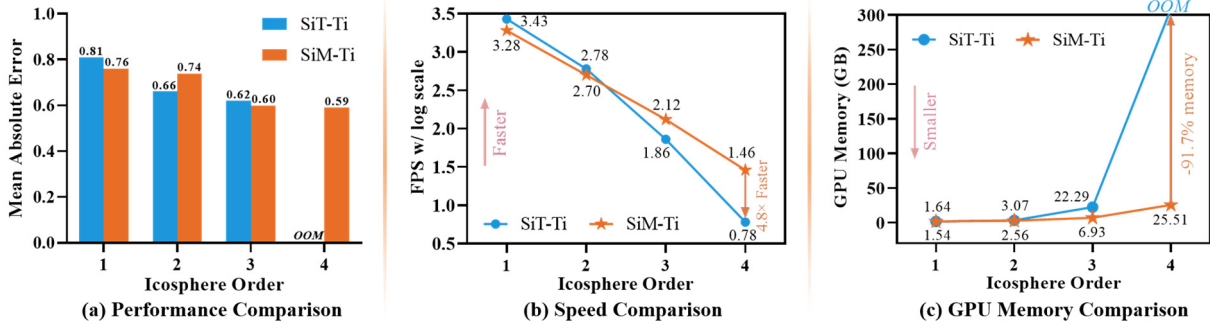


Figure 3. Comparison of PMA prediction performance and efficiency between SiT and our SiM.

Additionally, we conducted further experiments:

1. Ablation studies on the decoder design in autoregressive pretraining, the best performance is achieved when the decoder depth is 1 and the width is 256.
2. The impact of preterm birth on the brain development, we find that predicted brain age in preterm infants was significantly lower than chronological age in the *Subset 2*, with $MAE = 0.89 \pm 0.87$ and $MSE = 1.56 \pm 2.71$, suggesting that preterm birth may delay brain development at term-equivalent age.
3. Among all the models, SiM achieved the best performance in predicting Language (SiM-Base/2) and Motor (SiM-Small/1) outcomes at 18 months, with $MAE = 2.82 \pm 2.39$ and 1.55 ± 1.17 , and $MSE = 15.15 \pm 1.70$ and 2.32 ± 1.76 , respectively, when training from scratch.
4. Generalization validation experiment. We validate the generalization performance of model using *Replication dataset*. The results show that our SiM-Small/3 exhibits the best generalization performance with $MAE = 1.17 \pm 0.95$ and $MSE = 2.89 \pm 2.17$ when training with ImageNet pretraining weights, despite all results experiencing some decline.

The experiments mentioned above are provided in Appendix B and the parameter settings for all experiments are summarized in Appendix A.

4.3. Long Sequence and Efficiency Analysis

Figure 3a illustrates the performance and efficiency of the tiny-sized SiM model across different surface patching methods. In terms of MAE, SiM slightly outperforms SiT across all other patching methods except when using an Ico-2 grid, and both models exhibit decreasing MAE as the icosphere order increases. Regarding FPS (Frames Per Second), SiM is slightly slower than SiT when the icosphere order is below 3 but surpasses it as the order increases (Figure 3b). For GPU memory usage, SiM exhibits better efficiency with SiT when icosphere orders raises. Notably, when using an Ico-4 as grid, SiM is 4.8 times faster and consumes 91.7% less GPU memory compared to SiT (Figure 3c). All experiments on efficiency analysis are conducted on a 40G A100 device. These results highlight the suitability of SiM for finer-grained tasks and its potential for practical clinical applications.

4.4. Cortical Regions with Significant Contributions to Age Prediction

We perform a sensitive analysis [34] on the test dataset of *Subset 1* to evaluate the contribution of individual vertex on cortical surface to brain age prediction, as illustrated in Figure 4. For each vertex on the brain surface, we assessed four morphometric features (i.e., curvature, sulcal depth, cortical thickness, and myelination). "All" nullifies all features, while other results nullify one feature at a time per vertex. Contributions were quantified by measuring performance changes before and after nullification, with larger shifts indicating greater impact.

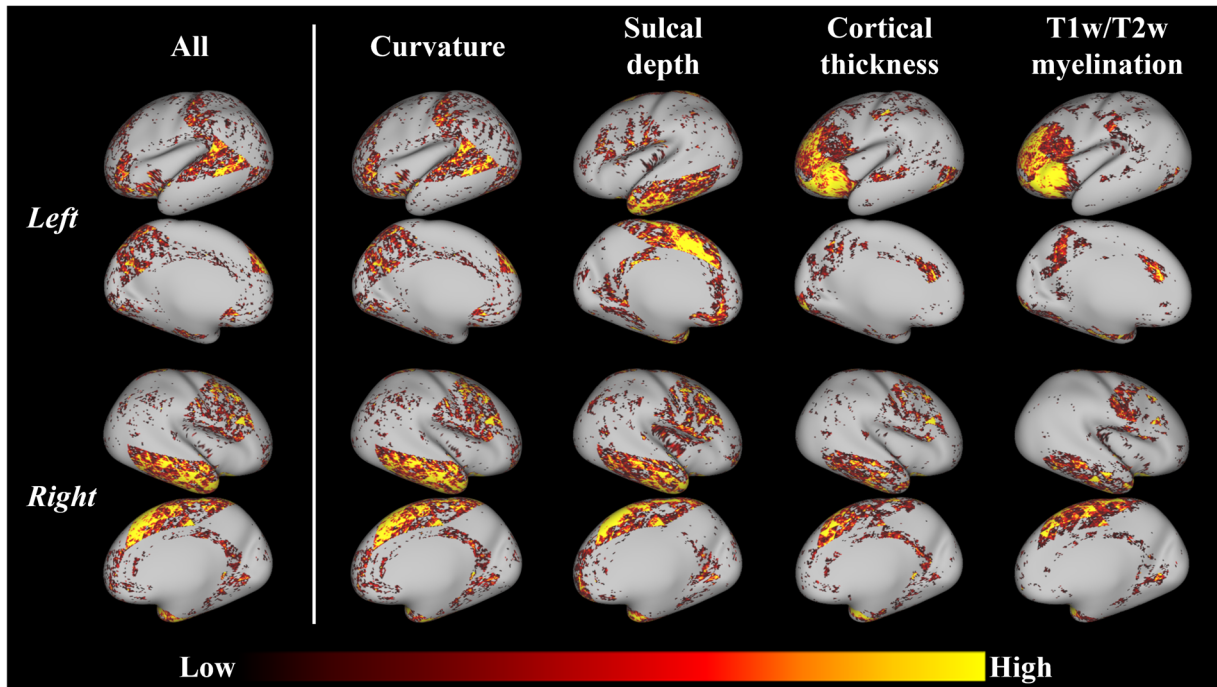


Figure 4. Spatial distribution of informative vertices for PMA prediction.

The mean performance change for each vertex/feature was computed, normalized using z-score, and visualized on the cortical surface (Figure 4). The intensity of the hot color signifies the influences of each vertex/feature. In the right hemisphere, key regions include the temporal lobe, precentral gyrus, and prefrontal and paracentral cortices. The left hemisphere shows a similar focus on the prefrontal cortex, sensory cortex, language areas, and parietal cortex when all features or only curvature are masked. Sulcal depth complements these findings by emphasizing the temporal lobe, central sulcus regions, and superior frontal and parietal areas. Cortical thickness and myelination highlight frontal regions, particularly the anterior insula, rostral middle frontal gyrus, and orbitofrontal cortex.

5. Conclusion

In this study, we introduced Surface Vision Mamba (SiM), a novel vision backbone with sub-quadratic time complexity, tailored for genus-zero surfaces. We validated SiM as a more robust and efficient alternative to SiT in the challenging task of neurodevelopmental phenotype prediction from cortical surface data. Leveraging the strengths of Mamba in handling *long-sequence* and *autoregressive modeling*, we extended sequence lengths using various surface patching methods and conducted autoregressive pretraining. While SiM demonstrated sensitivity to sequence length, the benefits of autoregressive pretraining were limited, likely due to constraints of small samples. The use of longer sequences facilitated finer-grained partitioning, enhancing the ability to identify potential pathological features critical in clinical applications. Furthermore, SiM offers faster inference speeds and lower GPU memory consumption, making it both efficient and practical. Sensitivity analysis also emphasized the interpretability of SiM, highlighting its potential utility in medical research and applications.

Reference

- [1] T. S. Cohen, M. Geiger, J. Köhler, and M. Welling, "Spherical cnns," *arXiv preprint arXiv:10130*, 2018.
- [2] M. Defferrard, X. Bresson, and P. Vandergheynst, "Convolutional neural networks on graphs with fast localized spectral filtering," *Advances in neural information processing systems*, vol. 29, 2016.
- [3] T. N. Kipf and M. Welling, "Semi-supervised classification with graph convolutional networks," *arXiv preprint arXiv:02907*, 2016.
- [4] C. R. Qi, L. Yi, H. Su, and L. J. Guibas, "Pointnet++: Deep hierarchical feature learning on point sets in a metric space," *Advances in neural information processing systems*, vol. 30, 2017.
- [5] S. Dahan *et al.*, "Surface vision transformers: Attention-based modelling applied to cortical analysis," in *International Conference on Medical Imaging with Deep Learning*, 2022: PMLR, pp. 282-303.
- [6] L. Zhao *et al.*, "An Attention-Based Hemispheric Relation Inference Network for Perinatal Brain Age Prediction," *IEEE Journal of Biomedical Health Informatics*, 2024.
- [7] V. Vosylius *et al.*, "Geometric deep learning for post-menstrual age prediction based on the neonatal white matter cortical surface," in *Uncertainty for Safe Utilization of Machine Learning in Medical Imaging, and Graphs in Biomedical Image Analysis: Second International Workshop, UNSURE 2020, and Third International Workshop, GRAIL 2020, Held in Conjunction with MICCAI 2020, Lima, Peru, October 8, 2020, Proceedings 2*, 2020: Springer, pp. 174-186.
- [8] A. Fawaz *et al.*, "Benchmarking geometric deep learning for cortical segmentation and neurodevelopmental phenotype prediction," *bioRxiv*, p. 2021.12.01.470730, 2021.
- [9] A. Gu, K. Goel, and C. Ré, "Efficiently modeling long sequences with structured state spaces," *arXiv preprint arXiv:00396*, 2021.
- [10] A. Gu and T. Dao, "Mamba: Linear-time sequence modeling with selective state spaces," *arXiv preprint arXiv:00752*, 2023.
- [11] A. Dosovitskiy, "An image is worth 16x16 words: Transformers for image recognition at scale," *arXiv preprint arXiv:11929*, 2020.
- [12] K. Han, Y. Wang, J. Guo, Y. Tang, and E. Wu, "Vision gnn: An image is worth graph of nodes," *Advances in neural information processing systems*, vol. 35, pp. 8291-8303, 2022.
- [13] L. Zhu, B. Liao, Q. Zhang, X. Wang, W. Liu, and X. Wang, "Vision mamba: Efficient visual representation learning with bidirectional state space model," *arXiv preprint arXiv:09417*, 2024.
- [14] W. Yu and X. Wang, "MambaOut: Do We Really Need Mamba for Vision?," *arXiv preprint arXiv:07992*, 2024.
- [15] F. Monti, D. Boscaini, J. Masci, E. Rodola, J. Svoboda, and M. M. Bronstein, "Geometric deep learning on graphs and manifolds using mixture model cnns," in *Proceedings of the IEEE conference on computer vision and pattern recognition*, 2017, pp. 5115-5124.
- [16] F. Zhao *et al.*, "Spherical U-Net on cortical surfaces: methods and applications," in *Information Processing in Medical Imaging: 26th International Conference, IPMI 2019, Hong Kong, China, June 2-7, 2019, Proceedings 26*, 2019: Springer, pp. 855-866.
- [17] A. Vaswani, "Attention is all you need," *Advances in Neural Information Processing Systems*, 2017.
- [18] J. D. M.-W. C. Kenton and L. K. Toutanova, "Bert: Pre-training of deep bidirectional transformers for language understanding," in *Proceedings of naacL-HLT*, 2019, vol. 1: Minneapolis, Minnesota, p. 2.

- [19] L. Floridi and M. Chiriatti, "GPT-3: Its nature, scope, limits, and consequences," *Minds Machines*, vol. 30, pp. 681-694, 2020.
- [20] Z. Liu *et al.*, "Swin transformer: Hierarchical vision transformer using shifted windows," in *Proceedings of the IEEE/CVF international conference on computer vision*, 2021, pp. 10012-10022.
- [21] S. Wang, B. Z. Li, M. Khabsa, H. Fang, and H. Ma, "Linformer: Self-attention with linear complexity," *arXiv preprint arXiv:04768*, 2020.
- [22] J. Qiu, H. Ma, O. Levy, S. W.-t. Yih, S. Wang, and J. Tang, "Blockwise self-attention for long document understanding," *arXiv preprint arXiv:02972*, 2019.
- [23] I. Han, R. Jayaram, A. Karbasi, V. Mirrokni, D. P. Woodruff, and A. Zandieh, "Hyperattention: Long-context attention in near-linear time," *arXiv preprint arXiv:05869*, 2023.
- [24] I. Beltagy, M. E. Peters, and A. Cohan, "Longformer: The long-document transformer," *arXiv preprint arXiv:05150*, 2020.
- [25] T. Dao, D. Fu, S. Ermon, A. Rudra, and C. Ré, "Flashattention: Fast and memory-efficient exact attention with io-awareness," *Advances in Neural Information Processing Systems*, vol. 35, pp. 16344-16359, 2022.
- [26] T. Dao, "Flashattention-2: Faster attention with better parallelism and work partitioning," *arXiv preprint arXiv:08691*, 2023.
- [27] J. Shah, G. Bikshandi, Y. Zhang, V. Thakkar, P. Ramani, and T. Dao, "Flashattention-3: Fast and accurate attention with asynchrony and low-precision," *arXiv preprint arXiv:08608*, 2024.
- [28] D. Han *et al.*, "Agent attention: On the integration of softmax and linear attention," in *European Conference on Computer Vision*, 2025: Springer, pp. 124-140.
- [29] D. Han *et al.*, "Demystify Mamba in Vision: A Linear Attention Perspective," *arXiv preprint arXiv:16605*, 2024.
- [30] S. Grossberg, "Recurrent neural networks," *Scholarpedia*, vol. 8, no. 2, p. 1888, 2013.
- [31] A. Gu, T. Dao, S. Ermon, A. Rudra, and C. Ré, "Hippo: Recurrent memory with optimal polynomial projections," *Advances in neural information processing* vol. 33, pp. 1474-1487, 2020.
- [32] Y. Liu *et al.*, "VMamba: Visual State Space Model," *arXiv preprint arXiv:11929*, vol. abs/2401.10166, 2024.
- [33] S. Ren *et al.*, "Autoregressive Pretraining with Mamba in Vision," *arXiv preprint arXiv:07537*, 2024.
- [34] A. Saltelli, "Sensitivity analysis for importance assessment," *Risk analysis*, vol. 22, no. 3, pp. 579-590, 2002.

Appendix A. Implementation Details

All the experiments are implemented with Python 3.10.13 and PyTorch library and conducted on 4 NVIDIA A100 GPUs with batch size of 32. The Vim-Tiny[†], Vim-Small[†] and Vim-Base weights are adapted to initialize our model that Vim-Tiny[†] and Vim-Small[†] are fine-tuned under long sequence but no open-source Vim-Base[†] to use. The autoregressive pretraining for all model variants is performed using an Ico-3 grid and fine-tuned on the sequence obtained from other partitioning methods.

A.1. PMA Prediction Experiments

We assess the performance of our models in PMA prediction using the *Subset 1* which is described in Table 1. For all the model variants and surface patching methods, all training details were presented explicitly in Table 5.

Table 5. Hyperparameters for all training strategies in PMA prediction. Specifically, scratch means that training from scratch, fine-tuning refers to using ImageNet pretraining weights in Vim. For self-supervised pretraining, AR means autoregressive. T, S, B represent tiny-size, small-size, base-size, respectively.

	<i>Scratch</i>			<i>Fine-tuning</i>			<i>AR Pretraining</i>			<i>AR Fine-tuning</i>		
	<i>T</i>	<i>S</i>	<i>B</i>	<i>T</i>	<i>S</i>	<i>B</i>	<i>T</i>	<i>S</i>	<i>B</i>	<i>T</i>	<i>S</i>	<i>B</i>
Epochs	1000			600			4000	3000	3000	600		
Batch size	32			32			32			32		
Optimizer	AdamW			AdamW			AdamW			AdamW		
Adam ϵ	1e-8			1e-8			1e-8			1e-8		
Adam (β_1, β_2)	(0.9, 0.999)			(0.9, 0.999)			(0.9, 0.999)			(0.9, 0.999)		
LR	5e-5			5e-5	5e-5	3e-5	1.5e-4			1.5e-4	1e-4	8e-5
LR decay	Linear			Linear			Cosine			Cosine		
Step size	500			200	200	500	-			-		
Gamma	0.5			0.5			-			-		
Gradient clipping	None			None			None			None		
Warmup epochs	None			None			10			10		
Weight decay	1e-8			1e-8			0.5			1e-6		
EMA decay rate	None			None			None			None		

A.2. Scaled Language Score Prediction Experiments

Predicting long-term language scores is a challenging task, directly applying the PMA recipe does not work. We find that it is no need for a long schedule and provide our recipe in Table 6.

Table 6. Hyperparameters for all training strategies in Scaled Language Score prediction.

	<i>Scratch</i>			<i>Fine-tuning</i>			<i>AR Pretraining</i>			<i>AR Fine-tuning</i>		
	<i>T</i>	<i>S</i>	<i>B</i>	<i>T</i>	<i>S</i>	<i>B</i>	<i>T</i>	<i>S</i>	<i>B</i>	<i>T</i>	<i>S</i>	<i>B</i>
Epochs	200	200	100	100			4000	3000	3000	300		
Batch size	32			32			32			32		
Optimizer	AdamW			AdamW			AdamW			AdamW		
Adam ϵ	1e-8			1e-8			1e-8			1e-8		
Adam (β_1, β_2)	(0.9, 0.999)			(0.9, 0.999)			(0.9, 0.999)			(0.9, 0.999)		
LR	8e-5	6e-5	6e-5	8e-5	8e-5	6e-5	1.5e-4			1.8e-4	1.2e-4	8e-5
LR decay	Cosine			Cosine			Cosine			Cosine		
Step size	-			-			-			-		
Gamma	-			-			-			-		
Gradient clipping	None			None			None			None		
Warmup epochs	10			10			10			10		
Weight decay	1e-4			1e-4			0.5			1e-6		
EMA decay rate	None			None			None			None		

A.3. Scaled Motor Score Prediction Experiments

The training setting is in Table 7 and we observe that this to be akin to language score prediction. It is worth noting that a large warmup epoch can improve performance in some cases.

Table 7. Hyperparameters for all training strategies in Scaled Motor Score prediction.

	<i>Scratch</i>			<i>Fine-tuning</i>			<i>AR Pretraining</i>			<i>AR Fine-tuning</i>		
	<i>T</i>	<i>S</i>	<i>B</i>	<i>T</i>	<i>S</i>	<i>B</i>	<i>T</i>	<i>S</i>	<i>B</i>	<i>T</i>	<i>S</i>	<i>B</i>
Epochs		300			200		4000	3000	3000		200	
Batch size		32			32			32			32	
Optimizer		AdamW			AdamW			AdamW			AdamW	
Adam ϵ		1e-8			1e-8			1e-8			1e-8	
Adam (β_1, β_2)		(0.9, 0.999)			(0.9, 0.999)			(0.9, 0.999)			(0.9, 0.999)	
LR	1e-4	8e-5	8e-5	6e-5	4e-5	4e-5		1.5e-4		2e-4	1.5e-4	1.2e-4
LR decay		Cosine			Cosine			Cosine			Cosine	
Step size		-			-			-			-	
Gamma		-			-			-			-	
Gradient clipping		None			None			None			None	
Warmup epochs	50	10	50		10			10		50	10	10
Weight decay		1e-4			1e-4			0.5			1e-6	
EMA decay rate		None			None			None			None	

Appendix B. Additional Results

B.1. Decoder Design

We use SiM-T/3 for decoder architectures ablation experiments on *subset 1*, the fine-tuning MAE and MSE are summarized in Table 8. We first vary the *decoder depth*, and find that deeper decoders decreased performance shown in Table 8a. We further increase the *decoder width* in Table 8b, finding that performance improved when the dimension increased to 256, and then decreased.

Table 8. Ablation on decoder architectures. The reconstruction target is normalized features of each vertex. Default settings are marked in gray.

blocks	MAE	MSE	dim	MAE	MSE
1	0.91±0.81	3.62±2.73	128	1.04±0.87	3.34±1.94
2	0.97±0.81	3.54±2.51	256	0.91±0.81	3.62±2.73
4	1.08±0.97	2.99±1.15	512	1.05±0.83	3.88±2.68

(a) Decoder depth.

(b) Decoder width.

B.2. Brain Development Analysis of preterm infant

To explore whether preterm birth affects brain development, we applied the SiM-S/3 (fine-tuned with ImageNet pretraining weights) to the *Subset 2*. The paired samples t-test was utilized to assess the difference between predicted brain age and chronological brain age. The result showed that predicted brain age in preterm infants was significantly lower than chronological age in the *Subset 2*, with $MAE = 0.89 \pm 0.87$ and $MSE = 1.56 \pm 2.71$, as shown in Figure 5 ($p < 0.01$). The finding suggest that preterm birth may delay brain development at term-equivalent age.

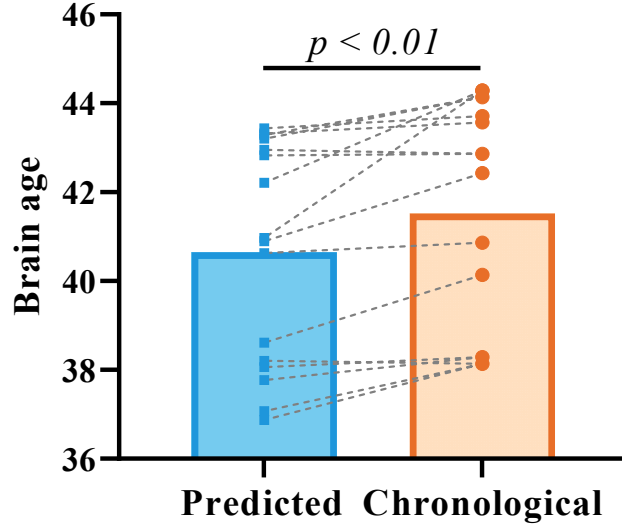


Figure 5. The significant difference between predicted and chronological brain age in preterm infants.

B.3. Infant Scaled Language and Motor Score Prediction

Table 9 and Table 10 shows the prediction results for language and motor scores, respectively. The proposed SiM achieved the best performance compared to other methods.

Table 9. Infant Scaled Language Score Prediction on *subset 3*.

Methods	Supervised		Fine-tuning		Autoregressive	
	MAE	MSE	MAE	MSE	MAE	MSE
MoNet	3.13±2.04	13.94±15.14	-	-	-	-
S2CNN	3.16±2.04	14.15±15.86	-	-	-	-
ChebNet	3.56±2.21	17.59±18.50	-	-	-	-
GConvNet	3.18±2.07	14.40±16.68	-	-	-	-
PointNet++	3.45±0.32	18.54±3.55	-	-	-	-
Spherical UNet	3.00±2.68	16.17±27.48	-	-	-	-
HRINet/1	3.38±2.09	29.48±15.50	-	-	-	-
SiT-Tiny/1	3.12±2.06	22.70±9.90	3.27±2.07	28.05±14.85	-	-
SiT-Small/1	3.25±2.04	24.67±11.24	3.31±1.96	21.86±8.00	-	-
SiT-Base/1	3.23±2.07	23.86±10.35	3.32±2.22	23.71±8.80	-	-
SiM-Tiny/1	3.22±2.29	21.34±6.48	3.12±2.30	15.74±0.82	3.55±2.38	29.62±12.82
SiM-Small/1	2.99±2.21	16.20±2.67	2.99±2.06	16.99±3.55	3.25±2.11	14.42±0.70
SiM-Base/1	2.91±2.47	13.63±1.02	3.05±2.15	17.83±4.44	3.28±2.19	18.84±3.77
HRINet/2	3.38±2.10	29.95±15.97	-	-	-	-
SiT-Tiny/2	3.22±2.06	28.50±12.09	3.41±2.01	28.64±14.70	-	-
SiT-Small/2	3.35±2.20	32.50±20.28	3.25±1.99	24.55±11.38	-	-
SiT-Base/2	3.11±2.03	22.84±10.30	3.38±2.07	28.52±14.56	-	-
SiM-Tiny/2	3.23±2.30	21.44±6.54	3.02±2.13	16.94±3.74	3.40±2.12	29.75±15.58
SiM-Small/2	3.19±2.25	15.52±4.87	3.02±2.23	18.66±5.18	3.39±2.17	32.27±18.23
SiM-Base/2	2.82±2.39	15.15±1.70	3.12±2.15	18.22±4.38	3.41±2.39	30.33±14.74
HRINet/3	<i>OOM</i>	<i>OOM</i>	-	-	-	-
SiT-Tiny/3	3.20±2.06	23.44±10.15	3.24±2.04	24.23±10.82	-	-
SiT-Small/3	3.20±2.06	23.20±9.85	3.24±2.13	25.70±12.06	-	-
SiT-Base/3	<i>OOM</i>	<i>OOM</i>	<i>OOM</i>	<i>OOM</i>	-	-
SiM-Tiny/3	3.04±2.14	17.64±4.29	3.03±2.13	17.35±4.07	3.36±2.12	29.74±15.81
SiM-Small/3	3.05±2.15	17.76±4.38	2.98±2.23	15.60±1.99	3.49±1.99	27.17±12.52
SiM-Base/3	3.02±2.00	14.91±2.02	2.90±2.30	16.49±3.19	3.46±2.43	19.37±1.67

Table 10. Infant Scaled Motor Score Prediction on *subset 3*.

<i>Methods</i>	<i>Supervised</i>		<i>Fine-tuning</i>		<i>Autoregressive</i>	
	MAE	MSE	MAE	MSE	MAE	MSE
MoNet	2.07±1.52	6.60±8.89	-	-	-	-
S2CNN	1.75±1.20	4.49±5.64	-	-	-	-
ChebNet	1.99±1.52	6.26±8.35	-	-	-	-
GConvNet	2.10±1.62	7.04±9.52	-	-	-	-
PointNet++	2.19±0.02	6.23±0.86	-	-	-	-
Spherical UNet	2.04±1.53	6.49±8.40	-	-	-	-
HRINet/1	1.78±1.27	2.72±2.50	-	-	-	-
SiT-Tiny/1	1.83±1.28	3.04±2.35	1.73±1.30	3.41±1.52	-	-
SiT-Small/1	1.78±1.26	2.77±2.39	1.88±1.29	3.27±2.31	-	-
SiT-Base/1	1.80±1.25	2.93±2.25	1.76±1.26	2.84±2.20	-	-
SiM-Tiny/1	1.75±1.19	2.57±2.33	1.63±1.19	2.35±2.07	1.74±1.25	2.62±2.40
SiM-Small/1	1.55±1.17	2.32±1.76	1.66±1.28	2.53±2.28	1.83±1.23	3.78±1.32
SiM-Base/1	1.56±1.22	2.52±1.71	1.80±1.32	2.82±2.58	1.72±1.31	3.10±1.90
HRINet/2	1.77±1.27	2.71±2.49	-	-	-	-
SiT-Tiny/2	1.73±1.26	2.71±2.25	1.88±1.27	3.14±2.42	-	-
SiT-Small/2	1.80±1.28	2.97±2.31	1.78±1.25	2.86±2.26	-	-
SiT-Base/2	1.81±1.27	3.00±2.30	1.97±1.21	3.79±1.86	-	-
SiM-Tiny/2	1.99±1.47	3.58±3.05	1.80±1.26	2.75±2.51	1.84±1.39	3.07±2.68
SiM-Small/2	1.84±1.33	3.19±2.38	1.78±1.42	3.57±1.95	1.94±1.50	3.38±3.18
SiM-Base/2	1.83±1.37	2.98±2.70	1.78±1.31	2.78±2.55	1.93±1.44	3.98±2.18
HRINet/3	<i>OOM</i>	<i>OOM</i>	-	-	-	-
SiT-Tiny/3	1.78±1.25	2.87±2.25	1.82±1.27	2.86±2.49	-	-
SiT-Small/3	1.80±1.25	2.96±2.25	1.76±1.26	2.88±2.18	-	-
SiT-Base/3	<i>OOM</i>	<i>OOM</i>	<i>OOM</i>	<i>OOM</i>	-	-
SiM-Tiny/3	2.00±1.68	3.75±3.73	1.79±1.27	2.94±2.24	1.80±1.33	2.84±2.63
SiM-Small/3	1.82±1.39	2.90±2.83	1.81±1.30	2.79±2.61	1.78±1.29	2.74±2.51
SiM-Base/3	1.84±1.40	3.01±2.82	1.70±1.25	2.54±2.31	1.92±1.45	3.27±3.04

B.4. Generalization validation

We validated the generalization for different models on the *Replication dataset*. The results indicate the performance of all the models decreased, but our SiM still demonstrated the best generalization performance with $MAE = 1.17 \pm 0.95$ and $MSE = 2.89 \pm 2.17$. All results are detailed in Table 11.

Table 11. Generalization validation on the *Replication dataset*.

Methods	Supervised		Fine-tuning		Autoregressive	
	MAE	MSE	MAE	MSE	MAE	MSE
MoNet	1.64±0.89	3.09±2.43	-	-	-	-
S2CNN	1.83±1.21	4.65±6.09	-	-	-	-
ChebNet	1.58±1.40	4.45±6.52	-	-	-	-
GConvNet	1.98±1.07	5.08±3.75	-	-	-	-
PointNet++	3.27±1.07	13.04±6.39	-	-	-	-
Spherical UNet	1.86±1.04	2.78±3.12	-	-	-	-
HRINet/1	8.61±1.88	77.63±30.35	-	-	-	-
SiT-Tiny/1	3.70±1.54	16.08±10.24	8.43±2.11	75.55±32.83	-	-
SiT-Small/1	3.41±1.34	13.40±9.51	4.02±1.09	17.33±8.98	-	-
SiT-Base/1	4.00±1.68	18.84±12.48	6.19±1.65	41.05±17.92	-	-
SiM-Tiny/1	4.32±1.75	20.05±9.68	5.72±2.16	36.81±11.64	3.85±1.62	15.74±7.50
SiM-Small/1	5.32±1.66	28.42±11.30	3.60±1.62	14.19±6.33	2.05±1.41	7.42±4.46
SiM-Base/1	4.81±1.69	24.03±10.03	3.78±2.97	20.06±21.66	1.63±1.47	6.59±6.33
HRINet/2	4.25±1.74	21.08±12.31	-	-	-	-
SiT-Tiny/2	2.90±1.32	10.13±7.32	4.88±1.84	27.16±14.99	-	-
SiT-Small/2	3.33±1.38	13.01±8.89	2.08±0.78	4.95±3.31	-	-
SiT-Base/2	2.72±1.45	9.50±8.43	4.73±1.75	25.49±13.24	-	-
SiM-Tiny/2	4.48±2.62	28.31±12.52	5.04±1.83	26.66±8.56	6.11±2.24	39.59±14.42
SiM-Small/2	4.66±1.77	23.88±8.53	2.01±0.96	5.52±2.14	4.12±1.63	18.06±8.10
SiM-Base/2	4.81±1.69	24.03±10.03	1.51±1.50	6.08±5.48	3.43±1.55	12.92±5.04
HRINet/3	-	-	-	-	-	-
SiT-Tiny/3	2.83±1.49	10.26±8.43	2.18±1.02	5.79±4.28	-	-
SiT-Small/3	2.91±1.44	10.53±8.37	1.86±0.99	4.43±3.89	-	-
SiT-Base/3	-	-	-	-	-	-
SiM-Tiny/3	5.44±1.72	25.09±12.40	1.56±0.97	4.11±2.61	3.54±1.24	13.09±4.92
SiM-Small/3	4.66±1.77	23.88±8.53	1.17±0.95	2.89±2.17	3.30±1.67	13.25±5.05
SiM-Base/3	4.36±1.76	21.48±7.48	1.61±1.08	3.65±0.89	4.26±1.89	19.40±8.06